

SAMv2: A Unified Framework for Learning Appearance, Semantic and Cross-Modality Anatomical Embeddings

Xiaoyu Bai, Fan Bai, Xiaofei Huo, Jia Ge, Jingjing Lu, Xianghua Ye, Ke Yan, and Yong Xia, *Member, IEEE*

Abstract—Identifying anatomical structures (e.g., lesions or landmarks) in medical images plays a fundamental role in medical image analysis. As an exemplar-based landmark detection method, Self-supervised Anatomical eMbedding (SAM) learns a discriminative embedding for each voxel in the image and has shown promising results on various tasks. However, SAM still faces challenges in: (1) differentiating voxels with similar appearance but different semantic meanings (e.g., two adjacent structures without clear borders); (2) matching voxels with similar semantics but markedly different appearance (e.g., the same vessel before and after contrast injection); and (3) cross-modality matching (e.g., CT-MRI registration). To overcome these challenges, we propose SAMv2, which is a unified framework designed to learn appearance, semantic, and cross-modality anatomical embeddings. Specifically, SAMv2 incorporates three key innovations: (1) semantic embedding learning with prototypical contrastive loss; (2) a fixed-point-based matching strategy; and (3) an iterative approach for cross-modality embedding learning. We thoroughly evaluated SAMv2 across three tasks, including one-shot landmark detection, lesion tracking on longitudinal CT scans, and CT-MRI affine/rigid registration with varying field of view. Our results suggest that SAMv2 outperforms SAM and other state-of-the-art methods, offering a robust and versatile approach for landmark based medical image analysis tasks. Code and trained models are available at: <https://github.com/alibaba-damo-academy/self-supervised-anatomical-embedding-v2>.

Index Terms—Anatomical embedding, landmark matching, multi-modality data alignment

I. INTRODUCTION

Identifying key anatomical structures (e.g. certain lesions or landmarks) from medical images plays a crucial role in the clinical workflow, as it helps with diagnosis, treatment planning, and other related procedures [1]–[3]. For instance,

This work was supported in part by the National Natural Science Foundation of China under Grants 62171377, and in part by the National Key R&D Program of China under Grant 2022YFC2009903 / 2022YFC2009900. (*Corresponding authors: Y. Xia*).

X. Bai and Y. Xia are with the National Engineering Laboratory for Integrated Aero-Space-Ground-Ocean Big Data Application Technology, School of Computer Science and Engineering, Northwestern Polytechnical University, Xi'an 710072, China (e-mail: yxia@nwpu.edu.cn).

J. Lu and X. Huo are with Beijing United Family Hospital, China.

X. Ye and J. Ge are with The First Affiliated Hospital, Zhejiang University, Hangzhou, China.

F. Bai is with the Department of Electronic Engineering, The Chinese University of Hong Kong, Hong Kong, China.

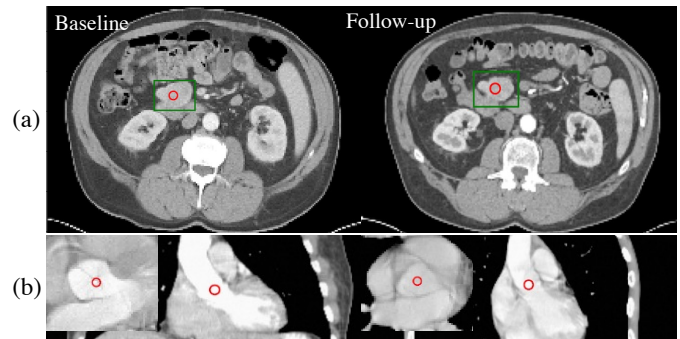


Fig. 1: Two examples of exemplar-based landmark detection. (a) In intra-patient case, an lesion annotation from one CT is used to locate the corresponding lesion on the follow-up scan. (b) In inter-patient case, an anatomical structure annotation (aortic valve) from one CT is used to identify the same anatomical structure of another subject.

doctors need compare the lesions between baseline and follow-up CT scans of the same subject to identify changes [4], [5]. Besides, in an image registration pipeline, two images need to be roughly aligned before deformable warping, which can be achieved by matching a set of landmarks on both images [6], [7]. Currently, most landmark detection methods rely on supervised learning [8]–[10], which requires manually annotated key points as supervision. Despite the high cost of manual annotation, these methods are limited to handle predefined landmarks and not able to detect arbitrary structures such as lesions.

Recently, a variety of methods have emerged for landmark detection using only a single exemplar annotation [11]–[13]. In these methods, landmark detection is formulated as a template-query matching problem, which aims to directly associate landmarks with exemplars based on their similarity in an anatomical embedding space. To achieve this, voxel-wise self-supervised learning pipelines are designed. Two augmented views of the same image are fed into a Siamese network to produce a dense feature map for each of them. The objective is to ensure that corresponding voxels in these two views render similar features, while non-corresponding voxels exhibit distinctive features. Given the inherent structural similarities in the human body across subjects, these methods are expected to produce similar features for the same anatomical structures

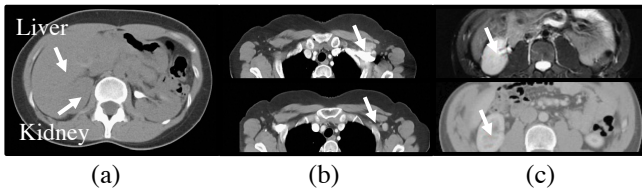


Fig. 2: Hard cases for self-supervised anatomical embeddings. (a) In a non-contrast CT, the liver and kidney exhibit similar texture and intensity distribution, making it difficult to distinguish them using self-supervised appearance features. (b) The use of contrast agents greatly alters the appearance of vessels, leading to confusion with ribs. (c) Matching anatomical structures across modalities (e.g. MRI and CT).

among different subjects. Consequently, the annotations from one subject can be leveraged as exemplars to locate the corresponding structures in other subjects.

One representative method within this context is the Self-supervised Anatomical eMbedding (SAM) [11], which can produce a unique embedding for each voxel in a medical image such as a CT or MRI image. During inference, the nearest-neighbor (NN) matching technique is employed to locate the desired landmark based on the exemplar annotation. This approach has demonstrated promising results across various challenging tasks, including lesion tracking in longitudinal CT scans [5], universal landmark matching (Fig. 1), and CT image registration [14], [15]. Despite its success, it still has two major limitations. First, the discriminatory ability of SAM stems from self-supervised similarity measures of contextual appearance. Hence it is difficult for SAM to distinguish the structures that share similar appearances but have different semantics (Fig. 2 (a)) and to match the structures with similar semantics but distinct appearances (Fig. 2 (b)). In such cases, SAM may produce significant matching errors. Second, SAM is unable to perform cross-modality anatomy matching, which limits its utility in cross-modality applications such as cross-modality lesion tracking and registration (Fig. 2 (c)).

To tackle these challenges, we propose SAMv2, a unified framework for learning appearance, semantic, and cross-modality embeddings. Compared to SAM, SAMv2 introduces three key novelties.

(1) Semantic embedding learning by prototypical supervised contrastive (SupCon) loss: To address the problem of similar appearance with difference semantics, we incorporate a semantic head to generate a semantic embedding vector for each voxel. The semantic head is trained using the prototypical SupCon loss, which is specifically designed to facilitate supervised contrastive learning at the voxel level. Notably, we train the semantic head using publicly available organ segmentation datasets, making it easily accessible and adaptable.

(2) Fixed-point-based matching: To address the problem of similar semantics showing different appearance, we propose a fixed-point-based iterative matching technique to replace the naive NN matching strategy. We leverage the relation between the target structure and its surrounding “stable” structures to produce more reliable matching.

(3) We propose a novel framework for cross-modality embedding learning, which is designed to learn the correspondences between unregistered multi-modality images of the same subject without any manual annotation, even when they exhibit large field-of-view (FOV) differences.

We evaluate SAMv2 on both single-modality and cross-modality tasks. The former includes tracking lesions in arbitrary organs of longitudinal CT scans [5] and landmark detection on CT images using a single exemplar [11]. The latter is cross-modality affine/rigid registration, with a specific focus on the scenarios with large FOV disparities among different modalities. On single-modality tasks, SAMv2 not only achieves a significant performance improvement over SAM (from 81.87% to 84.06%), but also outperforms state-of-the-art lesion tracking and exemplar-based landmark detection methods. On the cross-modality registration task, SAMv2 achieves significantly smaller mean distance errors than current methods (SAMv2: $5.1 \pm 2.2\text{mm}$, C2FViT [16]: $13.4 \pm 11.6\text{mm}$), showing remarkable robustness under the conditions of significant FOV disparity. When applied to the downstream task of multi-modal tumor segmentation, our automatic method outperforms human-assisted traditional registration approach. SAMv2 has also been integrated as the registration tool in our solution to the MICCAI Liver Lesion Diagnosis Challenge (LLD-MMRI2023)¹, where we secured the 2nd position. We have released the entire training and inference codes, together with easy-to-use demos and trained models to facilitate the community to build their applications with this useful anatomical embedding and matching tool.

II. RELATED WORK

A. Exemplar-based medical landmark detection

In exemplar-based (*i.e.* one-shot) landmark detection methods, landmark detection in medical images is formulated as a template-query matching problem, with a central reliance on defining metrics to assess the similarity between voxels in template and query images. Most methods involve contrastive learning, which has a proven ability to generate similar features for visually similar images [17], [18]. For instance, Yao et al. [12], [13] designed the Cascade Comparing to Detect (CC2D) method to generate similar embeddings at each location on an image and its augmentation and achieved promising results on X-ray datasets. Based on CC2D, Quan et al. [2] proposed the Sample Choosing Policy (SCP) method to select the most representative template image from a dataset. Chen et al. [19] developed the Local Discrimination (LD) method, which learns contrastive self-supervised dense embeddings and generates segmentation masks through clustering simultaneously. They achieved promising performance across several 2D medical image datasets.

SAM [11] extends exemplar-based medical landmark detection to 3D images like CT and MRI. It is designed to capture anatomical information at the voxel level and generate similar embeddings for corresponding body parts, thereby facilitating template-query matching. SAM employs a coarse-to-fine contrastive learning process, where the coarse level

¹<https://github.com/LMMMEng/LLD-MMRI2023>

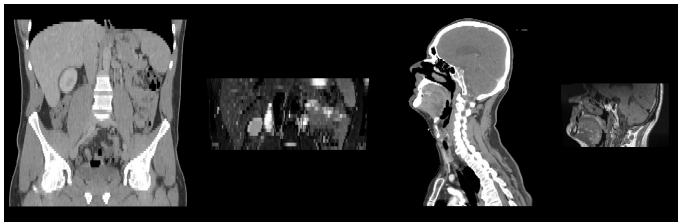


Fig. 3: Two examples of multi-modality medical images with substantially different FOVs. Left: Abdominal CT and MRI images; Right: Head and neck CT and MRI images.

learns global appearances, and the fine level learns local textures. Given a 3D image, SAM extracts two partially-overlapping patches and augments them through scaling and intensity transform. Voxels that appear in the same location on both patches are considered positive pairs, while other voxels (beyond a threshold to the positive pairs) on both patches are treated as negative samples. SAM deliberately selects hard and diverse negative samples to form the negative pairs. Finally, the InfoNCE loss [20] is applied to reduce the distance between positive pairs and push negative pairs apart. This results in all voxels on the 3D image having a distinct embedding representation and the same location on different augmented views having similar embeddings. Due to the high structural similarity of the human body across individuals, SAM can also output similar embeddings for the same anatomical structure on different subject’s scans. A recent study by Vitzitui et al. [21] showed that SAM may also benefit from the optional supervision, such as automatically extracted anatomical landmarks.

Essentially, these methods optimize the same objective, which is defined based on treating the same location on two augmented views as a positive pair and considering two different locations as a negative pair. Therefore, they share the weakness of SAM, whereas our approach is designed to address these weaknesses.

B. Multi-modality data alignment

The diagnostic accuracy can be significantly enhanced by utilizing the complementary information from aligned multi-modality medical images. A notable example is that the aligned MRI and CT images can empower radiotherapists for precise treatment planning [22]. Typically, multi-modality medical images are aligned in two steps: a global affine or rigid transformation [16], [23], [24] and a deformable registration [6], [25]. However, in our experiments, existing affine/rigid registration methods cannot work well when two images have substantially different FOVs (Fig. 3 and 9). In such circumstances, it is necessary to crop these two images into a similar FOV. This alignment issue can be addressed by exemplar-based landmark detection methods, which include matching sampled points on fixed and moving images followed by automatic image cropping. For single-modality images, SAME-affine [14], [15] leveraged SAM [11] to match corresponding points for affine registration, demonstrating impressive robustness in handling FOV differences. For multi-modality images,

however, training the SAM with cross-modality capabilities to drive SAME-affine may encounter a chicken-and-egg issue [7], since, on one hand, we require registered multi-modality images to train SAM and learn the correspondence and, on the other hand, we need the corresponding SAM landmarks for accurate image registration with a large FOV disparity.

Our solution to this chicken-and-egg issue involves a two-phase learning process. Initially, we train a single-modality SAM with aggressive contrast augmentation. This strategy is used to simulate the appearance difference in multi-modality images (e.g., CT and MRI). Subsequently, we use this aggressively augmented SAM as a seed to initiate an iterative process that alternates between cross-modality embedding learning and cross-modality registration. In the end, we obtain both a cross-modality SAM model and registered images. For new data, we can directly employ the trained cross-modality SAM for affine/rigid registration. The resulting images can then be fed into available deformable registration methods for voxel-wise alignment. By combining these two components, we create a robust, fully automated registration tool.

III. METHOD

The proposed SAMv2 consists of SAM++ and CrossSAM, which are designed for single- and multi-modality embedding learning, respectively. SAM++ can be further divided into two components: Semantic-SAM and fixed-point-based matching. The former is designed for appearance and semantic embedding learning, and the latter is a more reliable alternative for nearest neighbor (NN) matching. The illustrations of Semantic-SAM, fixed-point-based matching, and CrossSAM were displayed in Fig. 4, Fig. 5, and Fig. 6, respectively. We now delve into the details of each module.

A. Semantic-SAM

Semantic-SAM includes a semantic branch and an appearance branch, which share the same convolutional neural network (CNN) backbone (see Fig. 4 (a)). Note that we also tried to use transformer backbones but observed no significant performance gain. The appearance branch employs the same training strategy as the original SAM, where two overlapped and randomly augmented patches are fed into the CNN-backbone followed by the appearance head to generate the appearance embedding for each voxel. Let the embeddings of the positive pair be denoted by $\{\mathbf{x}_i, \mathbf{x}'_i\}$. The appearance branch aims to minimize the following voxel-wise contrastive loss

$$\mathcal{L}_{\text{app}} = - \sum_{i=1}^{n_{\text{pos}}} \log \frac{\exp(\mathbf{x}_i \cdot \mathbf{x}'_i / \tau_a)}{\exp(\mathbf{x}_i \cdot \mathbf{x}'_i / \tau_a) + \sum_{j=1}^{n_{\text{neg}}} \exp(\mathbf{x}_i \cdot \mathbf{x}_j / \tau_a)}, \quad (1)$$

where n_{pos} and n_{neg} denote the number of positive and negative pairs, respectively, and τ_a is the temperature parameter.

The self-supervised appearance head is able to learn the difference between two distinct body structures based on their appearances. However, it cannot distinguish challenging cases such as adjacent tissues and organs, which share similar intensity distribution and texture (see Fig. 2(a)). To overcome

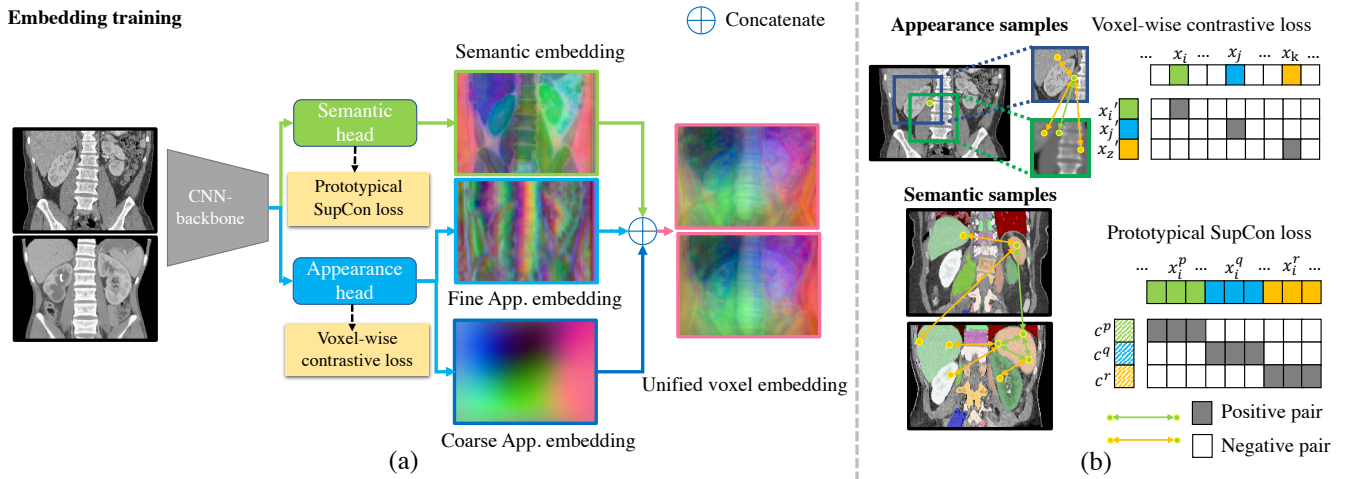


Fig. 4: Overview of Semantic-SAM. (a) Semantic-SAM contains a semantic head and an appearance head. The semantic head generates semantic embeddings, the appearance head is responsible for generating both coarse and fine appearance (App.) embeddings. The dimension of embeddings is reduced to 3 using PCA, and each embedding can be shown as a RGB image. (b) Illustration of voxel-wise contrastive loss and prototypical supervised contrastive loss, where x_i and x'_i are the embeddings of the same voxel on two augmented patches, and c^p and x_i^p represent the prototype and instance embeddings of class p .

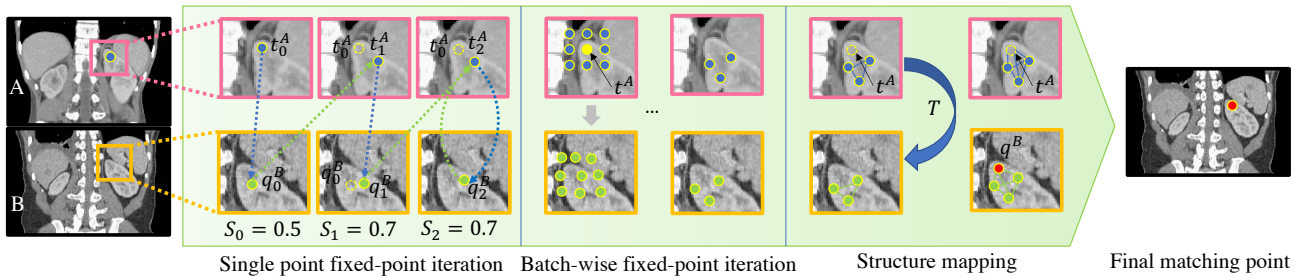


Fig. 5: Illustration of fixed-point-based matching method. We first show single point fixed-point iteration. Starting from the template point $t^A = t_0^A$, we identify a fixed point t_2^A with a high similarity score using iterative NN matching. The process is then extended to the grid points around t^A using batch-wise fixed-point iteration to obtain all fixed points (different starting points may converge to the same fixed point). Subsequently, we learn how the fixed points structure around t^A is mapped to the corresponding structure in B through an affine transform T . By considering t^A as an element of the fixed points structure in A , we can compute the matching point as $q^B = Tt^A$, which is more accurate and reliable than the initial NN matching result q_0^B .

this issue, we need higher-level semantic supervision to differentiate different tissues and organs.

We utilize a semantic branch to produce a fixed-length semantic embedding and treat it as a supplement to the appearance embedding. Our goal is to make the embeddings of the same organ closer than those from different organs. We can leverage any public organ segmentation dataset with arbitrary organ annotations. However, directly using the voxel-level supervised contrastive (SupCon) loss [26] is very expensive, since its complexity is $O(n^2)$, where n is the number of voxels in a patch ($\sim 300K$). To address this issue, we design a prototypical SupCon loss by replacing the voxel-voxel pairs with prototype-voxel pairs. During training, given the predicted embeddings produced by the semantic head $\{\mathbf{x}_i^p\}, i \in [1, n_p], p \in [1, K]$, where \mathbf{x}_i^p represents i th voxel embedding with semantic label p , n_p is the number of voxels with label p , K is the number of semantic classes (organs), we formulate the prototypical SupCon loss as

$$\mathcal{L}_s = \sum_{p=1}^K -\frac{1}{n_p} \sum_{i=1}^{n_p} \log \frac{\exp(\mathbf{c}_p \cdot \mathbf{x}_i^p / \tau_s)}{\sum_{q=1}^K \sum_{j=1}^{n_q} \exp(\mathbf{c}_p \cdot \mathbf{x}_j^q / \tau_s)}, \quad (2)$$

where $\mathbf{c}_p = \frac{1}{n_p} \sum_{i=1}^{n_p} \mathbf{x}_i^p$ is the prototype of class p , and τ_s is the temperature parameter. In contrast to the original SupCon loss, prototypical SupCon loss reduces the complexity from $O(n^2)$ to $O(nK)$, enabling its usage on dense prediction tasks. We apply the \mathcal{L}_2 normalization to the embeddings produced by both appearance and semantic heads, so that they can be directly concatenated and used as a unified embedding vector.

B. Fixed-point-based matching

After enhancing the anatomical embedding with semantic information, we also need a robust and accurate point matching strategy. The original SAM computes the inner product of template and query embeddings and uses NN matching. However,

when the target structure in the query image is missing or significantly altered (see Fig. 2(b)), this simple strategy may not be accurate.

Therefore, we propose an iterative structural inference method (see Fig. 5) to improve matching performance, which takes into account the consistency of a match and the relationship between the target landmark and its surrounding structures. Feeding two images A and B into SemanticSAM, we obtain the voxel embeddings $\mathbf{X}^A = \{\mathbf{x}_i^A\}$ and $\mathbf{X}^B = \{\mathbf{x}_i^B\}$, where i is the index of pixels. Let the template embedding vector on A be denoted by \mathbf{x}_t^A . We can find the corresponding query embedding on B through NN matching

$$\mathbf{x}_q^B = \operatorname{argmax}_{i \in B} (\mathbf{x}_t^A \cdot \mathbf{x}_i^B). \quad (3)$$

For simplicity, we ignore the notation of embedding \mathbf{x} and represent the template point and its NN matching point on B as: $t^A = t_0^A$ and q_0^B . We have established the correspondence $t_0^A \rightarrow q_0^B$. Let us consider the reverse process. Starting from q_0^B , can the NN matching method give us t_0^A ? If yes, we can conclude that we have a consistent forward-backward matching and that is probably a good matching. However, if the reverse process maps to another point, *i.e.*, $q_0^B \rightarrow t_1^A$ and $t_1^A \neq t_0^A$, then the first NN match is probably not reliable, since the similarity score of $S(q_0^B \rightarrow t_1^A)$ is larger than $S(q_0^B \rightarrow t_0^A)$.

Formally, the forward-backward process can be formulated as

$$t_{i+1}^A = f(t_i^A, \mathbf{X}^A, \mathbf{X}^B) \triangleq t_i^A \rightarrow q_i^B, q_i^B \rightarrow t_{i+1}^A. \quad (4)$$

Mathematically, a fixed point of a function is an element that is mapped to itself by the function [27]. Therefore, a forward-backward consistent matching identifies a fixed point of f since $t_0^A = t_1^A = f(t_0^A)$. For the matchings where $t_1^A \neq t_0^A$, although it is not a fixed point, we can always use it as a starting point to find a fixed point using the fixed-point iteration. Specifically, for any t_0^A , we compute a sequence of its f mappings

$$t_0^A, t_1^A = f(t_0^A), t_2^A = f(t_1^A), t_{i+1}^A = f(t_i^A), \dots \quad (5)$$

This process gradually increases the similarity score until, after n_{fix} iterations, the sequence converges to $t_{i+1}^A = t_i^A$ for all $i \geq n_{\text{fix}}$. In light of the fixed-point iteration, we propose an approach to locate the matching of t^A by considering all fixed points surrounding it. Our method begins with selecting an L^3 cubic region centered at the template point t^A and applying batched fixed-point iteration. Subsequently, we preserve fixed points with offsets to t^A below a threshold τ_{dis} . We treat these fixed points on image A as a structured element, and view their corresponding points on image B as another structure. We then estimate an affine transform T to describe their mapping relation. By including t^A in the fixed-point structure on A , we can compute the matching point as $q^B = Tt^A$. When a query point has a drastically different appearance, its NN matching result becomes unreliable. Our fixed-point based matching method can adaptively find highly reliable points surrounding the query point and aggregate this structural information to give the final matching result.

C. CrossSAM

In cross-modality scenarios, for example, we have a dataset comprising both CT and MRI images of each subject. Notably, each CT and MRI pair is not registered and could exhibit significant FOV differences, which is common in raw clinical data (CT scans often have larger FOV than MRI, see Fig. 3). We aim to learn cross-modality anatomical embeddings on this dataset, and thus find the correspondence between CT and MRI images. A straightforward solution is to register the CT and MRI images of each subject and then learn the cross-modality correspondence. Existing registration methods, however, can hardly deal with the image pair with significant FOV differences.

To address this issue, we propose an iterative approach named CrossSAM. Inspired by the idea of modality-agnostic learning [28], we first train a SAM model that is modality independent using strong or even aggressive contrast augmentation. Specifically, we randomly apply non-linear intensity transformation [29] and intensity reversal to each image. This process generates visually unrealistic intensity images (as shown in Fig. 6(a)), but it preserves the anatomical structures. Furthermore, we include the random affine transformation, resizing, and blurring in our augmentation pipeline. During training, we first pick one CT or MRI image randomly, crop two overlapping patches, then apply different aggressive augmentations to these two patches, and finally use them to train the SAM model. In this way, we force the model to learn the features that are independent of intensity and focus on higher-level structural similarity. As both CT and MRI are structural images, this SAM can roughly match the regions with strong structural information.

Nonetheless, directly using this aggressively augmented SAM for single-point matching is still locally inaccurate. Instead, we can estimate a reliable global affine/rigid transform from the matchings of multiple points. In SAME-affine [14], evenly spaced points were employed to calculate the affine matrix for two images. Since our CT-MRI pair is from the same subject, we favor computing the rigid transform matrix to prevent unwanted stretching. Our task is thus to solve a rigid fitting problem of two 3-D point sets. Given two 3-D point sets p_i and p'_i , $i = 1, \dots, N$, we assume

$$p'_i = Rp_i + t + n_i, \quad (6)$$

where R is a rotation matrix, t is a translation vector, and n_i is instance noise. We aim to find R and t that minimize

$$\Sigma^2 = \sum_{i=1}^N \|p'_i - (Rp_i + t)\|^2. \quad (7)$$

We utilize a quick and robust non-iterative method [30] to compute the rigid transfer matrix, which enables us to map the scan with a small FOV to its corresponding scan with a large FOV and crop the latter. Due to the potential inaccuracy of the rigid transfer, we dilate the body region of the small FOV scan to avoid the risk of cropping overlapping regions from two scans. After cropping the scan, both scans have similar FOVs. Then we apply a widely-used deformable registration

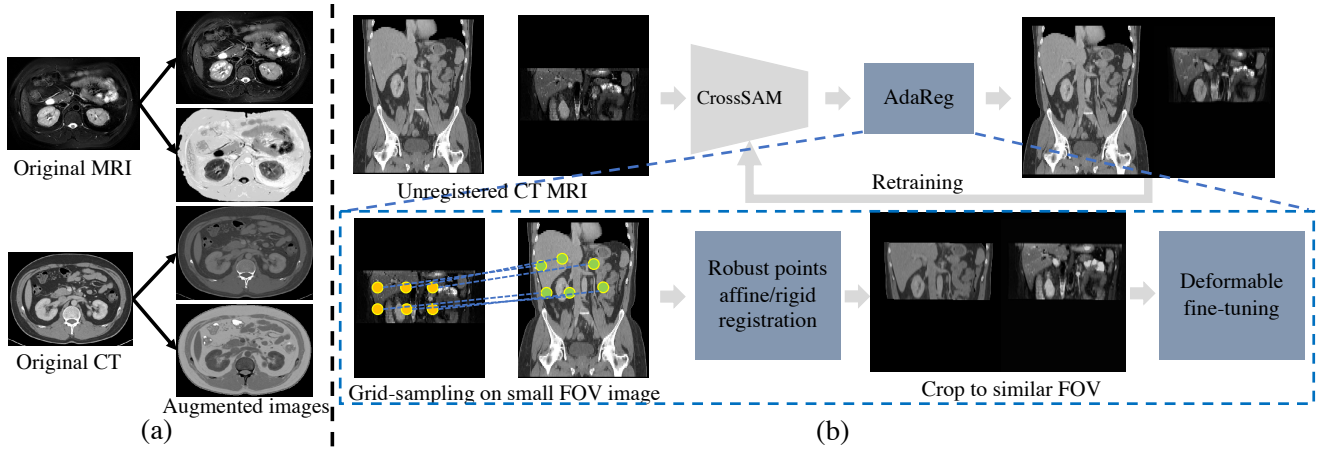


Fig. 6: Illustration of CrossSAM Framework. (a) shows the results of using aggressive intensity augmentation on MRI and CT images. (b) The iterative training procedure of CrossSAM.

method called DEEDS [31] to refine the results. This process is referred to as AdaReg (see Fig. 6 (b)).

After registering CT-MRI pairs using AdaReg, we can learn the cross-modality correspondence. For the fine-level learning, we select N_{pos}^f positive pairs from the registered regions with overlapping areas and choose N_{neg}^f points to act as negative samples. Additionally, we choose N_{fov}^f points from the non-overlapping area of the large FOV scan. Then the loss function is defined as

$$\mathcal{L} = - \sum_{i=1}^{N_{\text{pos}}^f} \log \frac{\exp(\mathbf{x}_i \cdot \mathbf{x}'_i / \tau_c)}{\exp(\mathbf{x}_i \cdot \mathbf{x}'_i / \tau_c) + \sum_{j=1}^{N_{\text{neg}}^f + N_{\text{fov}}^f} \exp(\mathbf{x}_i \cdot \mathbf{x}_j / \tau_c)}, \quad (8)$$

where x_i and x'_i are the embeddings of a positive pair, x_j represents the negative sample, and τ_c is a temperature parameter. Similarly, for the coarse-level learning, we select N_{pos}^c positive pairs and N_{neg}^c negative samples for each positive pair. To fully utilize the data, we also include augmented intra-modality data as input and using the self-supervised training method. However, as the alignment of CT-MRI pairs is based on the aggressive augmented SAM, erroneous correspondences may exist in imperfectly aligned cases. To improve the accuracy, we iterate the following two steps: run AdaReg using current CrossSAM embedding and learn CrossSAM with image pairs from AdaReg. In each iteration, we reduce the margin of the dilated body region of the small FOV image, resulting in a closer FOV for the cropped pairs and a more accurate deformable fine-tuning process. Our CrossSAM is obtained when this process converges after several iterations.

IV. EXPERIMENTS

A. Datasets

We trained SAM++ on two public datasets. The NIH-Lymph Node (NIH-LN) dataset [11] includes 176 chest-abdomen-pelvis CT scans, and the Total Segmentator dataset [32] contains 1204 CT images with the labels of 104 anatomical structures. We evaluated SAM++ on two tasks: lesion tracking and landmark detection using CT. The lesion tracking task aims to match the same lesion on longitudinal CT scans.

We used the publicly available deep longitudinal study (DLS) dataset [5], which contains 3008, 403, and 480 lesion pairs for training, validation, and testing, respectively. For landmark detection, we used the ChestCT dataset, which contains the contrast-enhanced (CE) and non-contrast (NC) CT scans of 94 subjects.

For CrossSAM, we use two in-house datasets for training and test. The head-and-neck (HaN) dataset consists of 120 paired T1 MRI and non-contrast CT images, which were not co-registered. Each MRI image has a voxel size of around $0.5 \times 0.5 \times 6 \text{ mm}^3$, and each CT image has a voxel size of around $1 \times 1 \times 3 \text{ mm}^3$. The MRI images have a limited FOV and mainly capture the region between the nose and the second cervical vertebra, while the CT images include the regions from the top of head to a portion of the lungs. We used 100 cases for training and reserved 20 for test. The abdomen (ABD) dataset contains 98 pairs of T2 MRI and non-contrast CT scans. The voxel sizes of CT and MRI images are $0.7 \times 0.7 \times 5 \text{ mm}$ and $0.8 \times 0.8 \times 8 \text{ mm}$, respectively. The MRI images have a small FOV that covers only a portion of liver and kidney, while the CT images encompass regions from the bottom of lung to the thighbone. We used 80 cases for training and 18 cases for test.

B. Performance Metrics

The accuracy of lesion tracking was assessed using the Center Point Matching (CPM) method [33], [34]. A match is deemed correct if the Euclidean distance between the predicted and ground truth centers is smaller than a threshold, which is set to either 10mm or the lesion radius [33], [34]. Other performance metrics are the Mean Euclidean Distance (MED) between the predicted and ground truth centers and its projections in each direction (referred to as MEDX, MEDY, and MEDZ). For the ChestCT landmark matching, we use the same setting as SAM by calculating the mean distance of 19 predefined landmarks using template-query matching.

We assessed the performance of cross-modality affine/rigid registration by comparing the voxel-level MED of the same landmark on the registered pairs. Specifically, we annotated 12

landmarks on both CT and MRI images on the HaN dataset, including the lacrimal gland, the endpoint of temporomandibular joint, the top and bottom of C2 spine, the middle point of jawbone, and the intersection of the lateral pterygoid muscle and upper jawbone. On the ABD dataset, we annotated 6 landmarks, including the top and bottom points of liver and spleen, as well as the top points of kidneys.

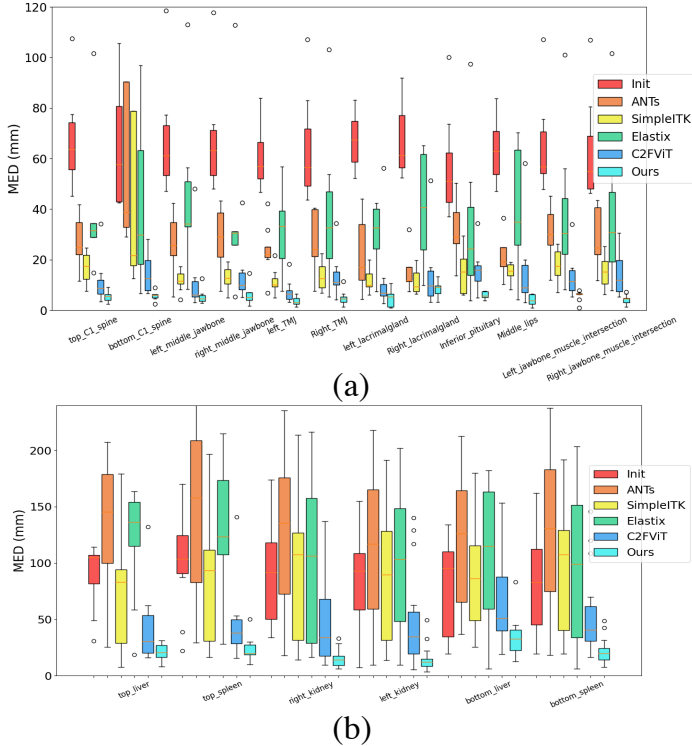


Fig. 7: Box-plot of the MED error of CT-MRI rigid registration on (a) HaN and (b) ABD datasets.

C. Implementation Details

The proposed SAMv2 was implemented using PyTorch v1.9 and MMDetection v1.20. We adopted 3D ResNet18 as our CNN-backbone and 3D feature pyramid network (FPN) as our semantic and appearance head. The embedding length of each head is set as 128. For the appearance head, we generated the coarse level embedding and fine level embedding. For the semantic head, we only generated the fine-level embedding. To save GPU memory, the size of output is the half of input volume size, we then used trilinear interpolation to re-slice the output to the original size. The network was optimized by SGD with a momentum of 0.9. The learning rate was set to 0.02, the batch size was set to 5, and the temperature τ_a and τ_s were set to 0.5. All CT volumes have been re-sliced to the isotropic resolution of $2 \times 2 \times 2$ mm³. For fixed-points matching, we set $L = 5$. We used random rotation, scaling (in $[0.8, 1.2]$), noise, and blurring for data augmentation. During training of CrossSAM, we iterated in each mini-batch with self-supervised learning and registered pair learning. For the self-supervised part, we cropped patches to a size of $96 \times 96 \times 32$ voxels and used a batch size of 4. For registered

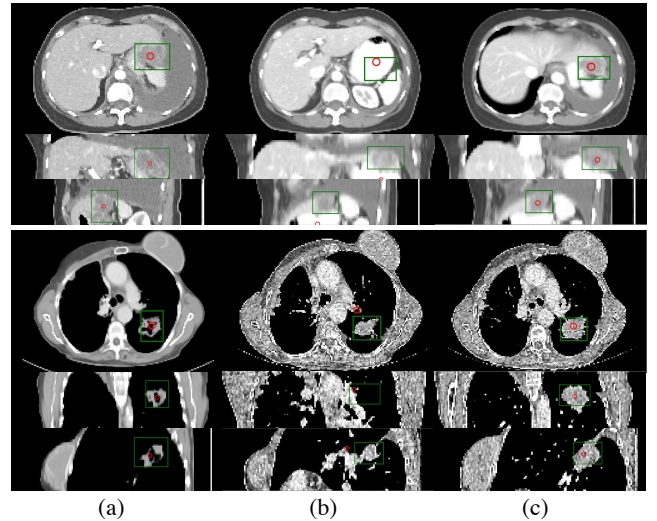


Fig. 8: A visual comparison of lesion tracking results of SAM and SAM++. We show two challenging cases with deformed organs and lesions, and altered contrast and image quality. Green boxes show the true lesion regions. Red circles indicate the true and tracked lesion centers. (a) Template (baseline) CT images. (b) and (c) are tracking results of SAM and SAM++ on the follow-up CT scan, respectively.

pairs, the input is the entire overlapped region along with a randomly selected region in the non-overlapped area. Due to the limited GPU memory, we only put one pair of data in each mini-batch. For fine-level embedding learning, we selected $N_{\text{pos}}^f = 200$ positive pairs, and, for each positive pair, we randomly selected $N_{\text{neg}}^f = 500$ and $N_{\text{fov}}^f = 100$ samples from the non-overlapped region. For coarse-level embedding learning, we set $N_{\text{pos}}^c = 100$, $N_{\text{neg}}^c = 200$, and $\tau_c = 0.5$.

D. Results

Table I displays the lesion tracking results on the DLS test set. We compared with supervised lesion tracking methods [4], [5], [33], [35], [36], registration methods [31], [37], [38], SAM [11] and the improved SAM [21]. It reveals that SAM++ outperforms all competing methods, though it does not use any task-specific supervision. Note that the organ masks used to train the semantic head contain no lesion information. The lesion tracking results produced by SAM and SAM++ were visualized in Fig. 8. It shows that the difficult cases for SAM can be effectively handled by SAM++.

Table II gives the performance of landmark detection on the ChestCT dataset. Previously in [11], the performance was examined exclusively on 19 test cases, focusing solely on intra-phase settings. By contrast, we conducted validation on all 94 cases, testing both intra- and inter-phase matching scenarios. It shows in Table II that the proposed SAM++ outperforms SAM across all settings consistently.

For the cross-modality registration task, we conducted a comprehensive comparison between our CrossSAM and C2FViT [16] and three widely used conventional affine/rigid registration methods (*i.e.*, ANTs [39], Elastix [40] and SimpleITK [41]). Among competing methods, C2FViT is a top-

TABLE I: Comparison of lesion tracking methods and our SAM++ on test set of DLS dataset.

Method	CPM@10mm (DLT- / TLT-Results)	CPM@Radius (DLT- / TLT-Results)	MED _X (mm)	MED _Y (mm)	MED _Z (mm)	MED (mm)
SiamRPN++, 2019 [35]	68.85/-	80.31/-	3.8 ± 4.8	3.8 ± 4.8	4.8 ± 7.5	8.3 ± 9.2
LENS-LesaNet, 2020 [4], [36]	70.00/-	84.58/-	2.7 ± 4.8	2.6 ± 4.7	5.7 ± 8.6	7.8 ± 10.3
DLT-Mix, 2021 [5]	78.65/-	88.75/-	3.1 ± 4.4	3.1 ± 4.5	4.2 ± 7.6	7.1 ± 9.2
DLT, 2021 [5]	78.85/-	86.88/-	3.5 ± 5.6	2.9 ± 4.9	4.0 ± 6.1	7.0 ± 8.9
TLT, 2022 [33]	-/87.37	-/95.32	3.0 ± 6.2	3.7 ± 5.2	1.7 ± 2.1	6.0 ± 7.7
Affine, 2016 [37]	48.33/-	65.21/-	4.1 ± 5.0	5.4 ± 5.6	7.1 ± 8.3	11.2 ± 9.9
VoxelMorph, 2018 [38]	49.90/-	65.59/-	4.6 ± 6.7	5.2 ± 7.9	6.6 ± 6.2	10.9 ± 10.9
DEEDS, 2013 [31]	71.88/-	85.52/-	2.8 ± 3.7	3.1 ± 4.1	5.0 ± 6.8	7.4 ± 8.1
SAM, 2022 [11]	81.87/86.14	91.56/95.41	2.6 ± 3.8	2.3 ± 2.9	4.0 ± 5.6	6.2 ± 6.9
Vizitiu et al., 2023 [21]	83.13/-	91.87/-	2.9 ± 6.0	2.2 ± 3.2	3.1 ± 3.9	5.9 ± 7.1
SAM++ (proposed)	84.06/89.27	93.02/96.77	2.3 ± 3.1	2.1 ± 2.7	3.6 ± 4.7	5.4 ± 5.7

†The methods in the upper part use lesion annotations in training, and thus have task-specific supervision. The methods in the lower part do not use lesion annotations. We observed discrepancies between the evaluation code presented in the TLT paper [33] and the DLT [5]. To ensure fairness, we report the results on both evaluation codes using the format of DLT-Results / TLT-Results.

TABLE II: Comparison of anatomical landmark detection methods and our SAM++ on ChestCT dataset. Same to original SAM [11] paper, we reported mean error ± std. and max error.

Method	CE-CE	NC-NC	CE-NC	NC-CE
On 19 test cases [11]				
Affine [37]	8.4±5.2 32.9	8.5±5.3 33.1	-	-
DEEDS [31]	4.6±3.3 18.8	4.7±3.4 24.4	-	-
VoxelMorph [38]	7.3±3.6 20.1	7.4±3.7 20.2	-	-
SAM [11]	4.3±3.0 16.4	4.5±3.0 18.5	-	-
On all 94 cases				
SAM [11]	4.8±3.4 23.6	4.6±3.5 25.9	4.7±3.5 44.0	5.2±3.9 29.6
SAM++	4.0±2.5 16.1	3.9±2.4 17.0	4.0±2.5 17.2	4.0±2.5 16.9

TABLE III: Ablation study of SAM++ on full DLS dataset [5] using evaluation code of TLT [33].

Method	CPM@ 10mm	CPM@ Radius	MED _X (mm)	MED _Y (mm)	MED _Z (mm)	MED (mm)
SAM [11]	88.94	93.44	2.4 ± 3.0	2.5 ± 3.1	3.6 ± 3.8	5.8 ± 5.0
SAM + Semantic head (Semantic-SAM)	89.37	93.99	2.3 ± 2.6	2.5 ± 2.8	3.5 ± 3.7	5.6 ± 4.5
SAM + Fixed-point-based matching	89.66	94.44	2.2 ± 2.4	2.3 ± 2.8	3.4 ± 3.7	5.3 ± 4.4
SAM++	91.05	95.45	2.2 ± 2.2	2.1 ± 2.2	3.2 ± 3.4	5.1 ± 3.8

performing learning-based registration approach, in which a local normalized cross-correlation (NCC) loss is utilized for intra-modality registration. Since the NCC loss may not be ideal for cross-modality scenarios, we followed the suggestion of the authors and replaced it with the local mutual information loss [42], [43] in our implementation of C2FViT. Since each CT-MRI pair is from the same subject, rigid registration is a more suitable choice. The box-plot results of rigid registration were depicted in Fig. 7. It shows that conventional methods struggle to handle the cases with significant FOV differences and hence yield poor performance in both HaN and ABD datasets. C2FViT stands out by reducing MED on both datasets. Our CrossSAM excels even further, consistently reducing MED for all landmarks on both datasets. It indicates that our CrossSAM is capable of providing a solid initial alignment for subsequent deformable registration in the highly challenging cross-modality and diverse-FOV scenario. The visualization of the registration results were shown in Fig. 9.

CrossSAM can be readily used in downstream tasks. We evaluated the performance of nasopharyngeal carcinoma (NPC) segmentation on the HaN dataset using CrossSAM as the initial affine step. The results were presented in Table IV. It show that our method outperforms manual cropping, enabling fully automated CT-MRI-based lesion segmentation.

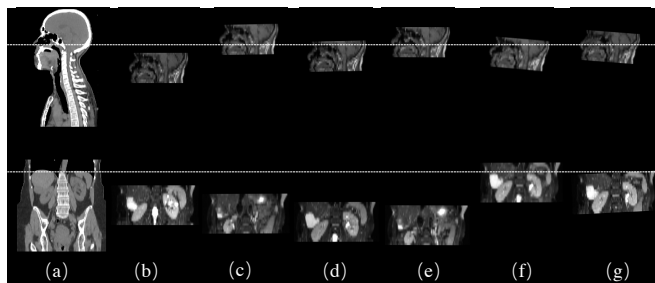


Fig. 9: Visualization of using different methods for rigid registration on HaN and ABD datasets. (a) Fixed images, (b) moving images, (c) Results of ANTs, (d) Results of Elastix, (e) Results of SimpleITK, (f) Results of C2FViT, and (g) Results of our CrossSAM.

CrossSAM has also been used to learn the correspondence on multi-phase MRI images. Fig. 10 shows an example of liver lesion matching on multi-phase MRI images from the LLD-MMRI challenge dataset. We achieved second place in the challenge thanks to the reliable performance of CrossSAM.

TABLE IV: Accuracy of nasopharyngeal carcinoma gross tumor volume (GTV) segmentation.

Method	HD95	Precision	Recall	Dice
CT-only	8.8±5.7	76.4±16.3	77.6±15.6	74.1±8.5
CT-MRI-M	8.5±4.8	79.2±15.4	75.9±14.6	75.0±8.2
CT-MRI-C	7.7±3.6	83.0±13.8	74.7±14.0	76.4±8.1

†CT-only means using only manually cropped CT to do segmentation. CT-MRI-M means manually cropping the CT volume for the rough region between the nose and the second cervical vertebra, followed by registering MRI to CT volume. CT-MRI-C denotes our CrossSAM method, which involves automatic cropping of the region based on the FOV of MRI volume. For all methods, we used DEEDS for deformable registration and nnUNet [44] for segmentation.

TABLE V: MED (mm) after each CrossSAM iteration on ABD dataset. Top row: CrossSAM rigid transform results. Bottom row: Adding DEEDS for deformable registration.

Initial	AggSAM	CrossSAM_0	CrossSAM_1
87.2 ± 39.6	35.8 ± 18.0	29.5 ± 14.9	25.7 ± 11.6
-	17.8 ± 17.2	11.8 ± 10.6	11.0 ± 9.1

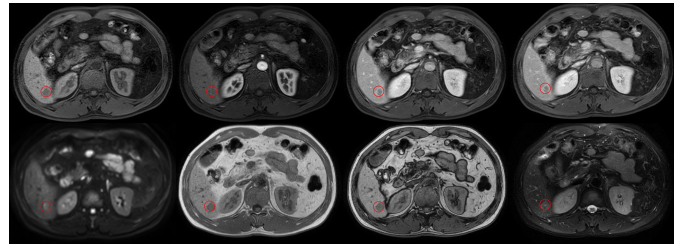
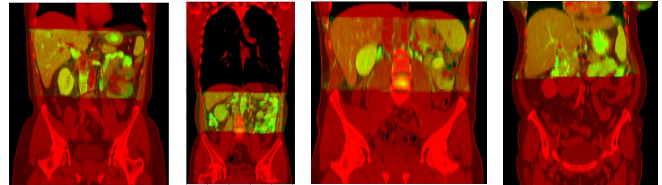
E. Ablation Study

Since we do not use DLS training set in model training, we conducted ablation study of SAM++ on the full DLS dataset. The results were presented in Table III. Note that SAM yields robust performance. By incorporating the semantic head, we enhance CPM@Radius from 93.44% to 93.99%. Additionally, by employing the fixed-point-based matching technique, we achieve a performance boost to 94.44%. These results demonstrate that both contributions we made in this work are effective. Finally, by combining these two techniques, the proposed SAM++ further improves CPM@Radius to 95.45%.

In Table V, we presented the overall MED of 6 landmarks on the ABD test set after each iteration for CrossSAM. The results reveal that the initial aggressive augmented SAM (AggSAM) significantly reduces the overall MED from 87 to 36mm. Through the utilization of the AdaReg + CrossSAM pipeline, after two retraining iterations, the final CrossSAM model reduces MED to 25.7mm. Adding deformable warping to DEEDS after the rigid registration step can further reduce MED. In Fig. 11, we show the examples of CrossSAM+DEEDS registration. These results suggest the effectiveness and robustness of the proposed method on cross-modality registration tasks.

V. CONCLUSION

Self-supervised exemplar-based landmark detection is an emerging topic as it does not need landmark annotations to train the model and can detect arbitrary anatomical points accurately and conveniently. Built upon the self-supervised anatomical embedding (SAM) framework [11], we propose SAMv2 to address the limitations of SAM, improving its accuracy and extending it to the multi-modality scenario. SAMv2 introduces three key innovations: (1) Semantic embedding learning with a prototypical supervised contrastive loss to equip the anatomical embeddings with semantic information; (2) A fixed-point-based structural matching mechanism for

**Fig. 10:** Lesion matching example using CrossSAM on eight MRI modalities from LLD-MMRI challenge.**Fig. 11:** Examples of cross-modality registration under FOV differences. MRI images (green) were overlaid on CT images (red).

more precise inference; and (3) A robust iterative pipeline for cross-modality anatomical embedding learning. SAMv2 has shown promising results on various medical image tasks, including lesion tracking in longitudinal CT scans, one-shot landmark detection, and cross-modality rigid registration with downstream tasks. We look forward to more applications to be developed with our released codes and models.

ACKNOWLEDGMENTS

The authors would like to thank Tony C. W. Mok, Zi Li, Minfeng Xu, Le Lu, and Dakai Jin for their invaluable help and suggestions.

REFERENCES

- [1] Y. Jiang, Y. Li, X. Wang, Y. Tao, J. Lin, and H. Lin, "Cephalformer: Incorporating global structure constraint into visual features for general cephalometric landmark detection," in *International Conference on Medical Image Computing and Computer-Assisted Intervention*. Springer, 2022, pp. 227–237.
- [2] Q. Quan, Q. Yao, J. Li, and S. K. Zhou, "Which images to label for few-shot medical landmark detection?" in *Proceedings of the IEEE/CVF Conference on Computer Vision and Pattern Recognition*, 2022, pp. 20 606–20 616.
- [3] Z. Zhong, J. Li, Z. Zhang, Z. Jiao, and X. Gao, "An attention-guided deep regression model for landmark detection in cephalograms," in *Medical Image Computing and Computer Assisted Intervention–MICCAI 2019: 22nd International Conference, Shenzhen, China, October 13–17, 2019, Proceedings, Part VI 22*. Springer, 2019, pp. 540–548.
- [4] K. Yan, J. Cai, Y. Zheng, A. P. Harrison, D. Jin, Y. Tang, Y. Tang, L. Huang, J. Xiao, and L. Lu, "Learning from multiple datasets with heterogeneous and partial labels for universal lesion detection in ct," *IEEE Transactions on Medical Imaging*, vol. 40, no. 10, pp. 2759–2770, 2020.
- [5] J. Cai, Y. Tang, K. Yan, A. P. Harrison, J. Xiao, G. Lin, and L. Lu, "Deep lesion tracker: monitoring lesions in 4d longitudinal imaging studies," in *Proceedings of the IEEE/CVF Conference on Computer Vision and Pattern Recognition*, 2021, pp. 15 159–15 169.
- [6] G. Balakrishnan, A. Zhao, M. R. Sabuncu, J. Guttag, and A. V. Dalca, "Voxelmorph: a learning framework for deformable medical image registration," *IEEE transactions on medical imaging*, vol. 38, no. 8, pp. 1788–1800, 2019.

- [7] Z. Yin, P. Gong, C. Wang, Y. Yu, and Y. Wang, "One-shot medical landmark localization by edge-guided transform and noisy landmark refinement," in *European Conference on Computer Vision*. Springer, 2022, pp. 473–489.
- [8] A. Q. O’Neil, A. Kaschenas, J. Henry, D. Wyeth, M. Shepherd, E. Beveridge, L. Clunie, C. Sansom, E. Seduikyte Keith Muir, and I. Poole, "Attaining human-level performance with atlas location autocontext for anatomical landmark detection in 3d ct data," in *Proceedings of the European Conference on Computer Vision (ECCV) Workshops*, 2018, pp. 0–0.
- [9] B. Bier, M. Unberath, J.-N. Zaech, J. Fotouhi, M. Armand, G. Osgood, N. Navab, and A. Maier, "X-ray-transform invariant anatomical landmark detection for pelvic trauma surgery," in *Medical Image Computing and Computer Assisted Intervention–MICCAI 2018: 21st International Conference, Granada, Spain, September 16–20, 2018, Proceedings, Part IV*. Springer, 2018, pp. 55–63.
- [10] H. Zhu, Q. Yao, and S. K. Zhou, "Datr: Domain-adaptive transformer for multi-domain landmark detection," *arXiv preprint arXiv:2203.06433*, 2022.
- [11] K. Yan, J. Cai, D. Jin, S. Miao, D. Guo, A. P. Harrison, Y. Tang, J. Xiao, J. Lu, and L. Lu, "Sam: Self-supervised learning of pixel-wise anatomical embeddings in radiological images," *IEEE Transactions on Medical Imaging*, vol. 41, no. 10, pp. 2658–2669, 2022.
- [12] Q. Yao, Q. Quan, L. Xiao, and S. Kevin Zhou, "One-shot medical landmark detection," in *Medical Image Computing and Computer Assisted Intervention–MICCAI 2021: 24th International Conference, Strasbourg, France, September 27–October 1, 2021, Proceedings, Part II 24*. Springer, 2021, pp. 177–188.
- [13] Q. Yao, J. Wang, Y. Sun, Q. Quan, H. Zhu, and S. K. Zhou, "Relative distance matters for one-shot landmark detection," *arXiv preprint arXiv:2203.01687*, 2022.
- [14] F. Liu, K. Yan, A. P. Harrison, D. Guo, L. Lu, A. L. Yuille, L. Huang, G. Xie, J. Xiao, X. Ye *et al.*, "Same: Deformable image registration based on self-supervised anatomical embeddings," in *Medical Image Computing and Computer Assisted Intervention–MICCAI 2021: 24th International Conference, Strasbourg, France, September 27–October 1, 2021, Proceedings, Part IV 24*. Springer, 2021, pp. 87–97.
- [15] Z. Li, L. Tian, T. C. Mok, X. Bai, P. Wang, J. Ge, J. Zhou, L. Lu, X. Ye, K. Yan *et al.*, "Samconvex: Fast discrete optimization for ct registration using self-supervised anatomical embedding and correlation pyramid," in *International Conference on Medical Image Computing and Computer-Assisted Intervention*. Springer, 2023, pp. 559–569.
- [16] T. C. Mok and A. Chung, "Affine medical image registration with coarse-to-fine vision transformer," in *Proceedings of the IEEE/CVF Conference on Computer Vision and Pattern Recognition*, 2022, pp. 20 835–20 844.
- [17] T. Chen, S. Kornblith, M. Norouzi, and G. Hinton, "A simple framework for contrastive learning of visual representations," in *International conference on machine learning*. PMLR, 2020, pp. 1597–1607.
- [18] M. Caron, I. Misra, J. Mairal, P. Goyal, P. Bojanowski, and A. Joulin, "Unsupervised learning of visual features by contrasting cluster assignments," *Advances in neural information processing systems*, vol. 33, pp. 9912–9924, 2020.
- [19] H. Chen, R. Wang, X. Wang, J. Li, Q. Fang, H. Li, J. Bai, Q. Peng, D. Meng, and L. Wang, "Unsupervised local discrimination for medical images," *IEEE Transactions on Pattern Analysis and Machine Intelligence*, 2023.
- [20] A. v. d. Oord, Y. Li, and O. Vinyals, "Representation learning with contrastive predictive coding," *arXiv preprint arXiv:1807.03748*, 2018.
- [21] A. Vizitiu, A. T. Mohaiu, I. M. Popdan, A. Balachandran, F. C. Ghesu, and D. Comaniciu, "Multi-scale self-supervised learning for longitudinal lesion tracking with optional supervision," in *International Conference on Medical Image Computing and Computer-Assisted Intervention*. Springer, 2023, pp. 573–582.
- [22] V. S. Khoo, E. J. Adams, F. Saran, J. L. Bedford, J. R. Perks, A. P. Warrington, and M. Brada, "A comparison of clinical target volumes determined by ct and mri for the radiotherapy planning of base of skull meningiomas," *International Journal of Radiation Oncology* Biology* Physics*, vol. 46, no. 5, pp. 1309–1317, 2000.
- [23] W. Huang, H. Yang, X. Liu, C. Li, I. Zhang, R. Wang, H. Zheng, and S. Wang, "A coarse-to-fine deformable transformation framework for unsupervised multi-contrast mr image registration with dual consistency constraint," *IEEE Transactions on Medical Imaging*, vol. 40, no. 10, pp. 2589–2599, 2021.
- [24] M. Hoffmann, B. Billot, D. N. Greve, J. E. Iglesias, B. Fischl, and A. V. Dalca, "Synthmorph: learning contrast-invariant registration without acquired images," *IEEE transactions on medical imaging*, vol. 41, no. 3, pp. 543–558, 2021.
- [25] T. C. Mok and A. C. Chung, "Large deformation diffeomorphic image registration with laplacian pyramid networks," in *Medical Image Computing and Computer Assisted Intervention–MICCAI 2020: 23rd International Conference, Lima, Peru, October 4–8, 2020, Proceedings, Part III 23*. Springer, 2020, pp. 211–221.
- [26] P. Khosla, P. Teterwak, C. Wang, A. Sarna, Y. Tian, P. Isola, A. Maschinot, C. Liu, and D. Krishnan, "Supervised contrastive learning," *Advances in neural information processing systems*, vol. 33, pp. 18 661–18 673, 2020.
- [27] A. Granas and J. Dugundji, *Fixed point theory*. Springer, 2003, vol. 14.
- [28] B. Billot, D. N. Greve, O. Puonti, A. Thielscher, K. Van Leemput, B. Fischl, A. V. Dalca, J. E. Iglesias *et al.*, "Synthseg: Segmentation of brain mri scans of any contrast and resolution without retraining," *Medical Image Analysis*, p. 102789, 2023.
- [29] Z. Zhou, V. Sodha, J. Pang, M. B. Gotway, and J. Liang, "Models genesis," *Medical image analysis*, vol. 67, p. 101840, 2021.
- [30] K. S. Arun, T. S. Huang, and S. D. Blostein, "Least-squares fitting of two 3-d point sets," *IEEE Transactions on pattern analysis and machine intelligence*, no. 5, pp. 698–700, 1987.
- [31] M. P. Heinrich, M. Jenkinson, M. Brady, and J. A. Schnabel, "Mrf-based deformable registration and ventilation estimation of lung ct," *IEEE transactions on medical imaging*, vol. 32, no. 7, pp. 1239–1248, 2013.
- [32] J. Wasserthal, M. Meyer, H.-C. Breit, J. Cyriac, S. Yang, and M. Segeroth, "Totalsegmentator: robust segmentation of 104 anatomical structures in ct images," *arXiv preprint arXiv:2208.05868*, 2022.
- [33] W. Tang, H. Kang, H. Zhang, P. Yu, C. W. Arnold, and R. Zhang, "Transformer lesion tracker," in *Medical Image Computing and Computer Assisted Intervention–MICCAI 2022: 25th International Conference, Singapore, September 18–22, 2022, Proceedings, Part VI*. Springer, 2022, pp. 196–206.
- [34] J. Cai, K. Yan, C.-T. Cheng, J. Xiao, C.-H. Liao, L. Lu, and A. P. Harrison, "Deep volumetric universal lesion detection using light-weight pseudo 3d convolution and surface point regression," in *International Conference on Medical Image Computing and Computer-Assisted Intervention*. Springer, 2020, pp. 3–13.
- [35] B. Li, W. Wu, Q. Wang, F. Zhang, J. Xing, J. S. Yan *et al.*, "Evolution of siamese visual tracking with very deep networks," in *Proceedings of the IEEE Conference on Computer Vision and Pattern Recognition, Long Beach, CA, USA, 2019*, pp. 16–20.
- [36] K. Yan, Y. Peng, V. Sandfort, M. Bagheri, Z. Lu, and R. M. Summers, "Holistic and comprehensive annotation of clinically significant findings on diverse ct images: learning from radiology reports and label ontology," in *Proceedings of the IEEE/CVF Conference on Computer Vision and Pattern Recognition*, 2019, pp. 8523–8532.
- [37] K. Marstal, F. Berendsen, M. Staring, and S. Klein, "Simpleelastix: A user-friendly, multi-lingual library for medical image registration," in *Proceedings of the IEEE conference on computer vision and pattern recognition workshops*, 2016, pp. 134–142.
- [38] G. Balakrishnan, A. Zhao, M. R. Sabuncu, J. Guttag, and A. V. Dalca, "An unsupervised learning model for deformable medical image registration," in *Proceedings of the IEEE conference on computer vision and pattern recognition*, 2018, pp. 9252–9260.
- [39] B. B. Avants, N. Tustison, G. Song *et al.*, "Advanced normalization tools (ants)," *Insight j*, vol. 2, no. 365, pp. 1–35, 2009.
- [40] S. Klein, M. Staring, K. Murphy, M. A. Viergever, and J. P. Pluim, "Elastix: a toolbox for intensity-based medical image registration," *IEEE transactions on medical imaging*, vol. 29, no. 1, pp. 196–205, 2009.
- [41] B. C. Lowekamp, D. T. Chen, L. Ibáñez, and D. Blezek, "The design of simpleitk," *Frontiers in neuroinformatics*, vol. 7, p. 45, 2013.
- [42] F. Maes, D. Vandermeulen, and P. Suetens, "Medical image registration using mutual information," *Proceedings of the IEEE*, vol. 91, no. 10, pp. 1699–1722, 2003.
- [43] J. Chen, E. C. Frey, Y. He, W. P. Segars, Y. Li, and Y. Du, "Transmorph: Transformer for unsupervised medical image registration," *Medical image analysis*, vol. 82, p. 102615, 2022.
- [44] F. Isensee, P. F. Jaeger, S. A. Kohl, J. Petersen, and K. H. Maier-Hein, "nnU-Net: A Self-Configuring Method for Deep Learning-Based Biomedical Image Segmentation," *Nature Methods*, vol. 18, no. 2, pp. 203–211, 2021.